

Hydrodynamics of a fish-like body undulation mechanism: Scaling laws and regimes for vortex wake modes

Cite as: Phys. Fluids **33**, 101904 (2021); <https://doi.org/10.1063/5.0062304>

Submitted: 04 July 2021 • Accepted: 22 September 2021 • Published Online: 14 October 2021

 Siddharth Gupta,  Atul Sharma,  Amit Agrawal, et al.



View Online



Export Citation



CrossMark

ARTICLES YOU MAY BE INTERESTED IN

[Body-caudal fin fish-inspired self-propulsion study on burst-and-coast and continuous swimming of a hydrofoil model](#)

Physics of Fluids **33**, 091905 (2021); <https://doi.org/10.1063/5.0061417>

[Flow map of foil undergoing combined fast and slow pitching](#)

Physics of Fluids **33**, 101902 (2021); <https://doi.org/10.1063/5.0063992>

[Active external control effect on the collective locomotion of two tandem self-propelled flapping plates](#)

Physics of Fluids **33**, 101901 (2021); <https://doi.org/10.1063/5.0065256>

Celebrate **Open Access Week** With



LEARN MORE



Hydrodynamics of a fish-like body undulation mechanism: Scaling laws and regimes for vortex wake modes

Cite as: Phys. Fluids **33**, 101904 (2021); doi: 10.1063/5.0062304

Submitted: 4 July 2021 · Accepted: 22 September 2021 ·

Published Online: 14 October 2021



View Online



Export Citation



CrossMark

Siddharth Gupta,^{1,2,3}  Atul Sharma,²  Amit Agrawal,²  Mark C. Thompson,¹  and Kerry Hourigan^{1,a)} 

AFFILIATIONS

¹Fluids Laboratory for Aeronautical and Industrial Research (FLAIR), Department of Mechanical and Aerospace Engineering, Monash University, Melbourne, Victoria 3800, Australia

²Department of Mechanical Engineering, Indian Institute of Technology Bombay, Mumbai 400076, India

³IITB-Monash Research Academy, IIT Bombay, Mumbai 400076, India

^{a)}Author to whom correspondence should be addressed: Kerry.Hourigan@monash.edu

ABSTRACT

A comprehensive two-dimensional numerical investigation has been undertaken to calculate the energetic cost of propulsion and the various flow transitions of a fish-like body undulation mechanism based on a National Advisory Committee for Aeronautics 0012 hydrofoil. This covers a wide range of Strouhal ($0 \leq St \leq 1.4$) and Reynolds ($500 \leq Re \leq 5000$) numbers from simulations based on a level-set function immersed-interface method. It is found that the time-averaged thrust coefficient displays a quadratic relationship with increasing St , and increases significantly with Re . Additionally, the time-averaged input power coefficient exhibits a cubic dependence with increasing St but is independent of Re . Both St dependences agree with those previously observed experimentally and numerically for an oscillating foil; however, for similar ranges of governing parameters, comparisons suggest that the body undulation mechanism possesses a higher propulsive efficiency. The $St \propto Re^{-0.19}$ scaling for the drag-to-thrust transition is consistent with that found for a wide variety of fish and birds in nature. Interestingly, for cases with an undulation wave-speed below the free-stream speed, the time-averaged drag coefficient is found to be higher than that of a stationary hydrofoil at the same Re . Furthermore, the time-averaged input power coefficient is negative, indicating the potential for the undulation mechanism to extract energy from the free-stream. Eight different wake patterns/transitions are documented for the parameter space; these have been assembled into a wake-regime parameter-space map. The present findings should aid in predicting and understanding different hydrodynamic forces and wake patterns for undulating kinematics.

Published under an exclusive license by AIP Publishing. <https://doi.org/10.1063/5.0062304>

I. INTRODUCTION

For decades, body undulations performed by anguilliform and carangiform type of body-and/or-caudal fin (BCF) fish have inspired engineers and scientists through their efficient modes of underwater propulsion. Thrust generation comes from periodic body bending in the form of a backward-traveling propulsive wave, leading to lateral undulations of their body and/or caudal-fin.^{1–4} Furthermore, in terms of propulsion efficiency and lateral stability, the literature suggests that this mechanism also outperforms other related propulsion mechanisms, for instance, pitching or oscillation of the caudal fin performed by thunniform BCF fish.^{5,6} Thus, the present numerical study focusses on examining the details of the body-undulation mechanism.

In terms of the flow physics of a two-dimensional (2-D) undulating streamlined body, the different non-dimensional parameters that govern

the fluid-structure system are: a hydrodynamical parameter—the Reynolds number (Re); kinematic parameters—the non-dimensional maximum amplitude at the tail (A_{max}), the non-dimensional wavelength (λ^*), and the non-dimensional undulation frequency (St); together with a geometrical parameter (body shape). The non-dimensional parameters are given by

$$Re = \frac{\rho u_\infty C}{\mu}, \quad St = \frac{2fa_{max}}{u_\infty}, \quad A_{max} = \frac{a_{max}}{C}, \quad \lambda^* = \frac{\lambda}{C}, \quad (1)$$

where ρ and μ are the density and dynamic viscosity of the surrounding fluid flowing at a constant free-stream velocity of u_∞ , C is the chord length of a NACA (National Advisory Committee for Aeronautics) hydrofoil, f is the frequency of undulation, and a_{max} is the maximum amplitude of undulation (measured) at the tail.

As a thrust generating mechanism for propulsion, many numerical, analytical, and computational studies have been performed to understand body undulations. One of the earlier studies exploring the undulation mechanism was performed by Lighthill.⁷ In this pioneering work, Lighthill concluded that the undulating body reaches its maximum propulsive efficiency when the wave speed of undulation matches or is close to the surrounding free-stream velocity. Liu *et al.*⁸ studied the flow pattern in the vicinity and wake of a NACA0012 hydrofoil, undulating with kinematics inspired by tadpoles, for different undulation frequencies $St = 0.33\text{--}0.62$ for $Re = 2100\text{--}11\,000$. Deng *et al.*⁹ performed two-dimensional simulations for a NACA0012 hydrofoil undulating at five different St , ranging from 0.2 to 1.0 in steps of 0.2, at $Re = 500$. For this parametric range, they observed that the hydrofoil reaches its maximum propulsive efficiency at $St = 0.8$. Dong and Lu¹⁰ investigated wake transitions and force coefficients at $Re = 5000$, for a NACA0012 hydrofoil undulating with a low St within the range 0–0.4. In two separate articles, Borazjani and Sotiropoulos^{11,12} studied the hydrodynamic performance of undulations inspired by carangiform and anguilliform fish. For undulation frequency $0 \leq St \leq 1.3$, and at three Reynolds numbers $Re = 300, 4000$, and ∞ , they observed that the critical St at which the transition from net drag to net thrust occurs is a decreasing function of Re . Yu *et al.*¹³ studied the hydrodynamic interactions of two foils in a tandem configuration. They observed that these foils could form stable configurations, separate, or collide with each other, depending on the amplitude and frequency ratios between them.

Recently, researchers also observed the power-harvesting capability of the undulation mechanism. One of the earlier studies on this novel energy-harvesting method was performed by Huang *et al.*¹⁴ They observed that an undulating body could harvest kinetic energy from flowing fluid if the non-dimensional wave speed $V_w = \lambda^* f / u_\infty$ lies in the range of 0.2–0.9. Following this, other studies were performed to understand the significance of different governing parameters, for instance, the Reynolds number;¹⁵ maximum amplitude, wavelength, and dimensionless wave velocity;¹⁶ and leading-edge radius.¹⁷ However, in most studies, the apparent fluid-dynamic mechanism for power harvesting was not discussed in detail.

The above literature survey shows that the undulation mechanism provides potential beyond the thrust generation mechanism used by BCF fish for locomotion. Most previous studies have been performed over narrow ranges of St and Re , since they were targeted toward understanding the swimming performance of fish, which undulate at $0.25 \leq St \leq 0.35$.¹⁸ Despite this, it is still worthwhile, from both a fundamental and applied point-of-view, to better understand the undulation mechanism, especially at very low St . As an efficient underwater propulsion mechanism, this can be used to fulfill the different needs of modern underwater vehicles. Further, the mechanism can also be used for harvesting energy from a surrounding fluid flow, especially at low Re , where the performance of traditional rotary turbines falls sharply.¹⁹ Thus, the objective of the present numerical study is to perform a parametric investigation on an undulating NACA0012 hydrofoil covering the broad ranges of $St = 0\text{--}1.4$ and $Re = 500\text{--}5000$. For an undulating hydrofoil, although Yu and Huang²⁰ performed a scaling analysis for the thrust coefficient, the present study aims for comprehensive scaling laws involving both thrust and power. The scalings are then compared with other bio-inspired propulsion mechanisms such as pitching and pitching/

heaving of an oscillating rigid foil. Next, the study proceeds to analyze the fluid dynamics behind the two capabilities of body undulation by which it switches from thrust generation (power consumption) at $V_w > 1$ to power harvesting at $V_w < 1$. Finally, the study focuses on understanding the different transitions in the force coefficients and the wake as St and Re are varied, especially at very low St , which have yet to be studied in detail.

II. METHODS: MODELING AND SIMULATIONS

A. Undulation kinematics and parametric details

The kinematics of undulations chosen for the present parametric investigation is inspired by the actual kinematics of a carangiform fish, based on the experimental work of Videler and Hess.²¹ This is given by

$$\Delta y(x, t) = a(x) \sin\left(\frac{2\pi x}{\lambda} - 2\pi ft\right), \quad (2)$$

where x is the streamwise distance measured along the chord from the leading edge of the hydrofoil, Δy is the lateral excursion of the hydrofoil at time t , $a(x)$ is the streamwise varying amplitude envelope of the undulation, λ is the wavelength of the wave traveling along the chord length, and f is the frequency of undulation. By considering the free-stream velocity u_∞ as the velocity scale, and the chord length C as the length scale, the non-dimensional form of Eq. (2) and the associated hydrofoil velocity V_{body} ⁶ are given as

$$\Delta Y(X, \tau) = A(X) \sin\left[2\pi\left(\frac{X}{\lambda^*} - \frac{St\tau}{2A_{max}}\right)\right], \quad (3)$$

$$V_{body}(X, \tau) = \frac{\pi St}{A_{max}} A(X) \cos\left[2\pi\left(\frac{X}{\lambda^*} - \frac{St\tau}{2A_{max}}\right)\right], \quad (4)$$

where $X = x/C$ and $Y = y/C$ are the non-dimensional coordinates in the streamwise and lateral directions, respectively; $A(x) = a(x)/C$ is the non-dimensional amplitude envelope; and $\tau = tu_p/C$ is the non-dimensional time. Furthermore, St , A_{max} , and λ^* [already defined in Eq. (1)] are the non-dimensional forms of frequency, maximum amplitude at the tail tip and wavelength of undulation, respectively.

For a carangiform-like undulation, the non-dimensional wavelength of undulation $\lambda^* = 1$ and the amplitude envelope $A(X)$ varies quadratically along the chord length^{11,21} given as

$$A(X) = a_0 + a_1 X + a_2 X^2, \quad (5)$$

with the coefficients $a_0 = 0.02$, $a_1 = -0.08$, and $a_2 = 0.16$; with the range of motion shown in Fig. 1(a). This figure shows that the maximum amplitude of undulations, $A_{max} = 0.1$, occurs at the tail tip, while the minimum amplitude occurs at approximately 0.23C (measured from the leading edge of the hydrofoil). Figure 1(b) shows the lateral displacement ΔY of the midline of the hydrofoil undulating with the carangiform kinematics, calculated using Eqs. (3) and (5) at several time instants within one undulation cycle. The figure shows that the combination of the quadratic amplitude envelope $A(X)$ and $\lambda^* = 1$ leads to restricted undulations for the anterior as compared to the posterior 1/3 part of the hydrofoil, which undulates at a higher amplitude.

For the present parametric numerical investigation, the non-dimensional input governing parameters A_{max} and λ^* are kept

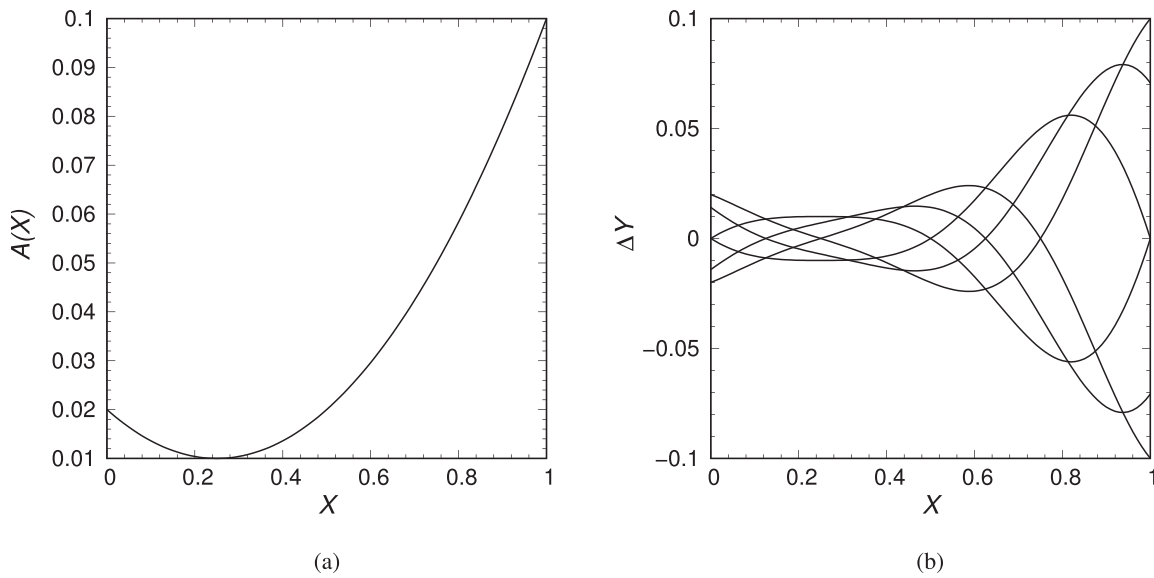


FIG. 1. Variation of (a) amplitude $A(X)$ [Eq. (5)] and (b) lateral displacement ΔY [Eq. (3)] along the chord of the hydrofoil. The ΔY is shown, for the centerline of the hydrofoil, at various time instants for one undulation cycle.

constant (similar to carangiform fish) while Re and St are varied over wide ranges as follows:

$$\text{Reynolds Number} = Re \left(\frac{\rho u_\infty C}{\mu} \right) : 500, 1000, 2000, 5000,$$

$$\text{Strouhal Number} = St \left(\frac{2fa_{max}}{u_\infty} \right) : 0 \text{ to } 0.2 \text{ (in steps of } 0.05), \\ 0.3 \text{ to } 1 \text{ (in steps of } 0.1), 1.2 \text{ and } 1.4$$

Here, $St=0$ corresponds to a stationary hydrofoil in a free-stream flow. The various non-dimensional propulsive output performance parameters considered in the study are the thrust coefficient C_T , viscous thrust coefficient C_{TV} , pressure thrust coefficient C_{TP} , input power coefficient C_P , and propulsive efficiency η_p , defined as

$$C_T = \frac{F_T}{1/2\rho u_\infty^2 C}, \quad C_{TV} = \frac{F_{TV}}{1/2\rho u_\infty^2 C}, \quad C_{TP} = \frac{F_{TP}}{1/2\rho u_\infty^2 C}, \quad (6)$$

$$C_P = \frac{\int c_L V_{body} dS}{1/2\rho u_\infty^3 C}, \quad \eta_p = \frac{P_{out}}{P_{in}} = \frac{\bar{F}_T u_\infty}{\int c_L V_{body} dS} = \frac{\bar{C}_T}{\bar{C}_P}, \quad (7)$$

where F_T is the thrust force (net force acting in the streamwise direction), F_{TV} is the viscous thrust force, and F_{TP} is the pressure thrust force. Furthermore, c_L is the local lateral force coefficient per unit surface area of the hydrofoil, and V_{body} is the lateral velocity of an undulating hydrofoil [Eq. (4)]. The propulsive efficiency η_p is defined⁶ as the ratio of the output power to the input power, where an overbar represents mean quantities obtained through time-averaging over a sufficiently large number of undulation cycles. Note that the above propulsive efficiency η_p is for most of the present net-thrust cases while an extraction efficiency η_{ex} is presented below for the few cases with net drag, and the efficiency for the free-swimming cases (at St_{cr} ,

defined differently in the literature^{11,22,23}) is not presented here. Further, for the cases with net thrust, the above definition of η_p is similar in all the three underwater propulsion kinematics (undulation, pitching, and pitching as well as heaving) commonly used for a hydrofoil.

The definitions of different non-dimensional output performance parameters are similar for both propulsion and energy extraction, except for the efficiency. For energy extraction, the extraction efficiency η_{ex} is generally expressed similarly to the so-called ‘‘Betz efficiency’’ for a rotary turbine as the ratio of the time-average net power absorbed to the power available in the flow that passes through the swept area of the foil,²⁴ given as

$$\eta_{ex} = \frac{\bar{P}_{ab}}{P_a} = \frac{\int c_L V_{body} dS}{1/2\rho u_\infty^3 2A_{max}} = \bar{C}_P \frac{C}{2A_{max}}. \quad (8)$$

B. Governing equations and numerical details

For an undulating hydrofoil, Ji and Huang¹⁵ showed a good agreement between the experimental and 2-D numerical predictions up to $Re \approx 50\,000$. Furthermore, various two-dimensional numerical simulations reported in the literature have successfully elucidated various characteristics of the body undulation mechanism within the present range of Re .^{6,10,25} Thus, for the largest Re of 5000 simulated here, 2-D numerical investigation of flow across an undulating hydrofoil is performed using an in-house code based on a level-set function-based immersed interface method (LS-IIM), proposed by Thekkethil and Sharma.²⁶ In this method, the temporal variation of the fluid–solid interface is tracked by using a level-set function ϕ , which is defined as a normal signed distance function from the interface. A positive value of ϕ represents the fluid cells, whereas a negative value represents the cells of solid. The method involves the direct application of the

boundary conditions at the interface, using the level-set function ϕ . The values of ϕ are calculated and updated for each time step by using minimum distance and winding algorithms, governed by the predefined kinematics of undulation (discussed in Subsection II A).

The fluid dynamics of the present one-way coupled fluid-structure interactions (FSIs) problem is governed by the kinematics of undulation and the incompressible Navier–Stokes equations, given by

$$\text{Continuity : } \nabla \cdot \vec{U} = 0, \tag{9}$$

$$\text{Momentum : } \frac{\partial \vec{U}}{\partial \tau} + \vec{U} \cdot (\nabla \vec{U}) = -\nabla P + \frac{1}{Re} \nabla^2 \vec{U}, \tag{10}$$

where $\vec{U} (\equiv \vec{u}/u_\infty)$ is the non-dimensional velocity vector and $P (\equiv p/\rho u_\infty^2)$ is the non-dimensional pressure.

The LS-IIM is a finite-volume-based method that utilizes a fully implicit pressure projection method on a collocated grid. The advection term of the Navier–Stokes equation is treated here by using the QUICK scheme, and the central difference scheme is used for the diffusion term. Further details and testing/validation of the implemented method are provided in Refs. 6 and 26.

C. Computational model and boundary conditions

Figure 2 shows the computational domain along with the boundary conditions for the present problem on flow across an undulating NACA0012 hydrofoil. The computational domain is non-dimensionalized by the chord length of the foil C and the free-stream velocity u_∞ . At the inlet, a constant velocity boundary condition is assigned. The lateral boundaries are $4C$ away from the hydrofoil with free-slip boundary conditions, providing a lateral blockage ($= 0.12C/8C$) of 1.5%, suggesting no significant effect of the lateral dimension on the hydrodynamics of undulation. The outlet boundary is $11C$ downstream of the head of the foil, and is assigned a convective boundary condition with convective velocity $U_c = 1$. The hydrofoil is considered as non-deforming (i.e., no flow-induced deformation) and a no-slip boundary condition is applied at its surface. The domain size was decided after a domain-size-independence study.

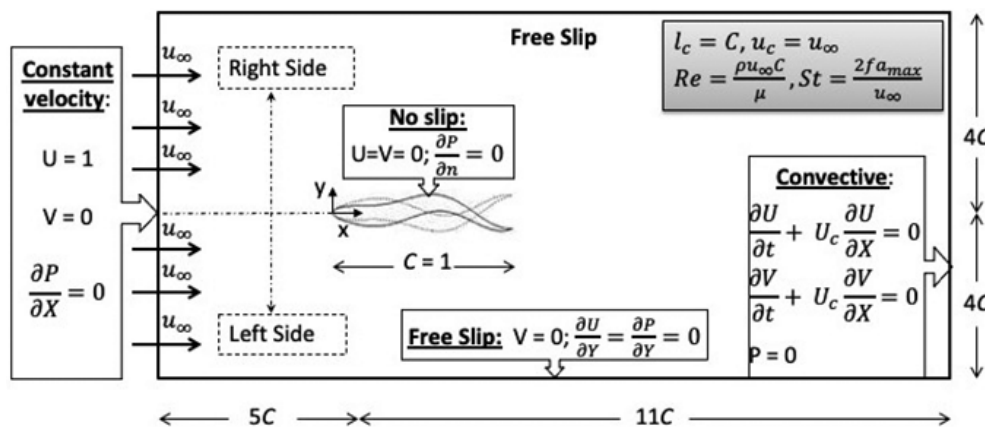


FIG. 2. Non-dimensional computational setup for an undulating NACA0012 hydrofoil in a free-stream flow.

D. Code validation, grid and domain independence

Verification and validation studies of the present in-house code for various one- and two-way coupled 2D/3D fluid-structure interaction (FSI) problems can be found in Thekkethil *et al.*,⁶ Thekkethil and Sharma,²⁶ Thekkethil *et al.*^{27,28} Figure 3(a) presents code validation for the present problem studied here. This shows excellent agreement with the results of Dong and Lu¹⁰ for the temporal variation of the thrust coefficient C_T and lateral force coefficient C_L of a NACA0012 hydrofoil, at $\lambda^* = 1$, $St = 0.4$, $A_{max} = 0.1$, and $Re = 5000$.

A grid independence study was also performed here considering three different Cartesian grid sizes: 382×142 , 768×314 , and 1543×588 , with uniform finest cell sizes of $\delta = [(\Delta x/C)_{min} = (\Delta y/C)_{min}] = 0.01, 0.005, \text{ and } 0.0025$ (used near the hydrofoil) stretching to a uniform coarse cell size of $\Delta = 0.5, 0.25, \text{ and } 0.125$ far away from the hydrofoil, respectively. The finest and coarsest grid spacings are connected using a hyperbolic stretching function. For a temporal variation of the lateral force coefficient C_L over a cycle of undulation of the NACA0012 hydrofoil at $\lambda^* = 1$, $St = 1.4$, $A_{max} = 0.1$, and $Re = 5000$, Fig. 3(b) shows no significant visual difference in the predicted lift coefficients for the three grids. To quantify this further, the difference between the maximum time-instantaneous C_L s between the two finest grids is approximately 2%. All further simulations in the present parametric investigation were performed using the intermediate grid size of 768×314 , noting that it has 200 points across the hydrofoil chord.

Finally, a domain independence study is carried out for two computational domains: $16C \times 8C$ and $16C \times 10C$ for the hydrofoil undulating at maximum governing parameters considered in the study, i.e., $St = 1.4$ and $Re = 5000$. The results for the time-averaged thrust and lift coefficient are compared and shown in Table I. The table shows that the difference in predicted lift from the two computational domains is $\sim 0.3\%$, with the difference in thrust considerably less. Thus, the computational domain of $16C$ in the streamwise direction and $8C$ in the lateral direction is considered for the present parametric investigation.

III. SCALING LAWS FOR HYDRODYNAMIC FORCES AND PROPULSIVE EFFICIENCY

Figure 4(a) depicts the mean thrust coefficient \bar{C}_T as a function of St for the range of Re considered in the study. At $St = 0$, when the

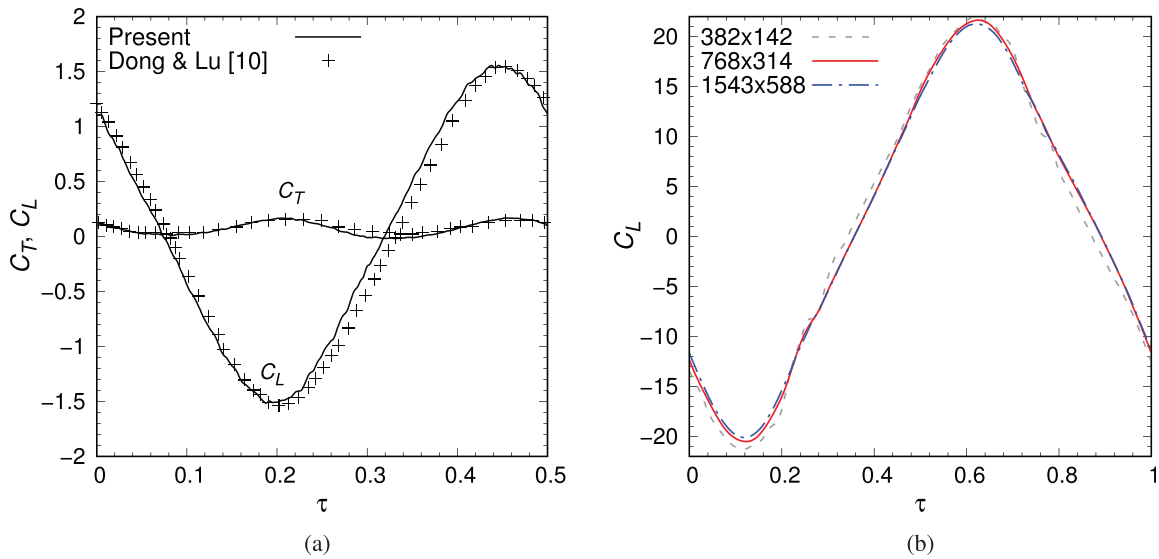


FIG. 3. (a) Code verification and (b) grid independence studies: Temporal variation of (a) thrust coefficient, C_T , and (a) and (b) lateral force coefficient, C_L , for a NACA0012 hydrofoil undulating at $\lambda^* = 1$, and $Re = 5000$. The Strouhal number, St , is 0.4 for (a) and 1.4 for (b).

hydrofoil is stationary, the negative value of \bar{C}_T in the figure shows that the foil experiences a net mean drag force, represented by \bar{C}_{Do} , which decreases with increasing Re . The mathematical relationship between the variation of \bar{C}_{Do} with Re can be given in the form $\bar{C}_{Do} = 4(Re)^{-0.5}$, as shown in Fig. 4(b), which shows a strong dependence of the net mean drag force with the Reynolds number, for the stationary hydrofoil. A similar relationship has also been observed by Das *et al.*²⁹ for Re ranging from 10 to 2000.

Considering the undulating motion at lower $0.05 \leq St \leq 0.15$, the figure shows that the net drag acting on the foil is larger than when the foil is stationary (these cases are associated with undulation with $V_w < 1$ and discussed in detail in Sec. IV). With a further increase in St , the net drag acting on the hydrofoil decreases, and then a crossover from net mean drag to net mean thrust occurs after reaching a critical Strouhal number, St_{cr} . One can observe from the figure that this St_{cr} is a function of Re and reduces with an increase in Re . For example, $St_{cr} \approx 0.5$ for $Re = 500$, which reduces to $St_{cr} \approx 0.33$ for $Re = 5000$. The corresponding relationship can be given as $St_{cr} = 1.64(Re)^{-0.19}$, as shown by curve fit in Fig. 4(b). Further, by comparing the present scaling with the data provided by Gazzola *et al.*³⁰ for $500 \leq Re \leq 5000$, it is interesting to observe from Fig. 4(b) that the derived scaling for St_{cr} lies within the range of actual St found for various amphibians, larvae, fish, marine birds, and mammals in nature. However, it should be noted that the derived relationship is based on body undulations for a carangiform fish, whereas the data are for

different species of flying or swimming living creatures that may use seemingly unrelated propulsion mechanisms. The decreasing function of St_{cr} with Re was also observed by Borazjani and Sotiropoulos¹¹ for a mackerel (carangiform) fish. However, as compared to the present study, they observe a larger $St_{cr} = 1.08, 0.6,$ and 0.26 for $Re = 300, 4000,$ and ∞ , respectively, indicating the significance of difference in the body shape between the two studies. Thus, for particular kinematics, St_{cr} is a function of both Re and the undulating hydrofoil/body shape.

With further increase in St (beyond St_{cr}), the net mean thrust coefficient generated by the hydrofoil increases and it is interesting to observe that the whole \bar{C}_T curve is close to quadratic with its minimum value at $St = 0.05$ for the range of St considered in our study. Furthermore, notice that the quadratic behavior is independent of the Reynolds number. However, the magnitude does differ with Reynolds number. For a deeper understanding of the quadratic nature of these curves, the net mean-thrust/drag has been divided into its pressure and viscous components and discussed separately below.

Figure 4(c) illustrates the first component of \bar{C}_T , the non-dimensional mean pressure thrust coefficient \bar{C}_{TP} , as a function of St for the range of Re considered in the study. The figure shows that \bar{C}_{TP} increases, after an initial reduction up to $St = 0.1$, with an increase in St . Interestingly, one can observe from the figure that all the curves for different Re collapse to a single curve. This shows that \bar{C}_{TP} does not depend on the Re . Also, notice that the curve is approximately quadratic in nature, i.e., $\bar{C}_{TP} \sim St^2(1 - 0.25/St)$, indicating the curve is non-monotonic with increasing St , and tends to St^2 at higher St . A similar relationship of $\bar{C}_{TP} \sim St^2$ has also been reported by Das *et al.*²⁹ for a pitching rigid hydrofoil. A similar scaling relation for the undulating and pitching hydrofoil, with a difference in the amplitude envelope, indicates that the amplitude envelope has an insignificant effect on relation for \bar{C}_{TP} . For larger St (cases with positive \bar{C}_{TP}), the reason for this quadratic variation can be given by the scaling analysis

TABLE I. Domain size independence study.

Domain size	\bar{C}_T	\bar{C}_L
16C × 8C	2.492 3	1.194 0
16C × 10C	2.492 2	1.191 4

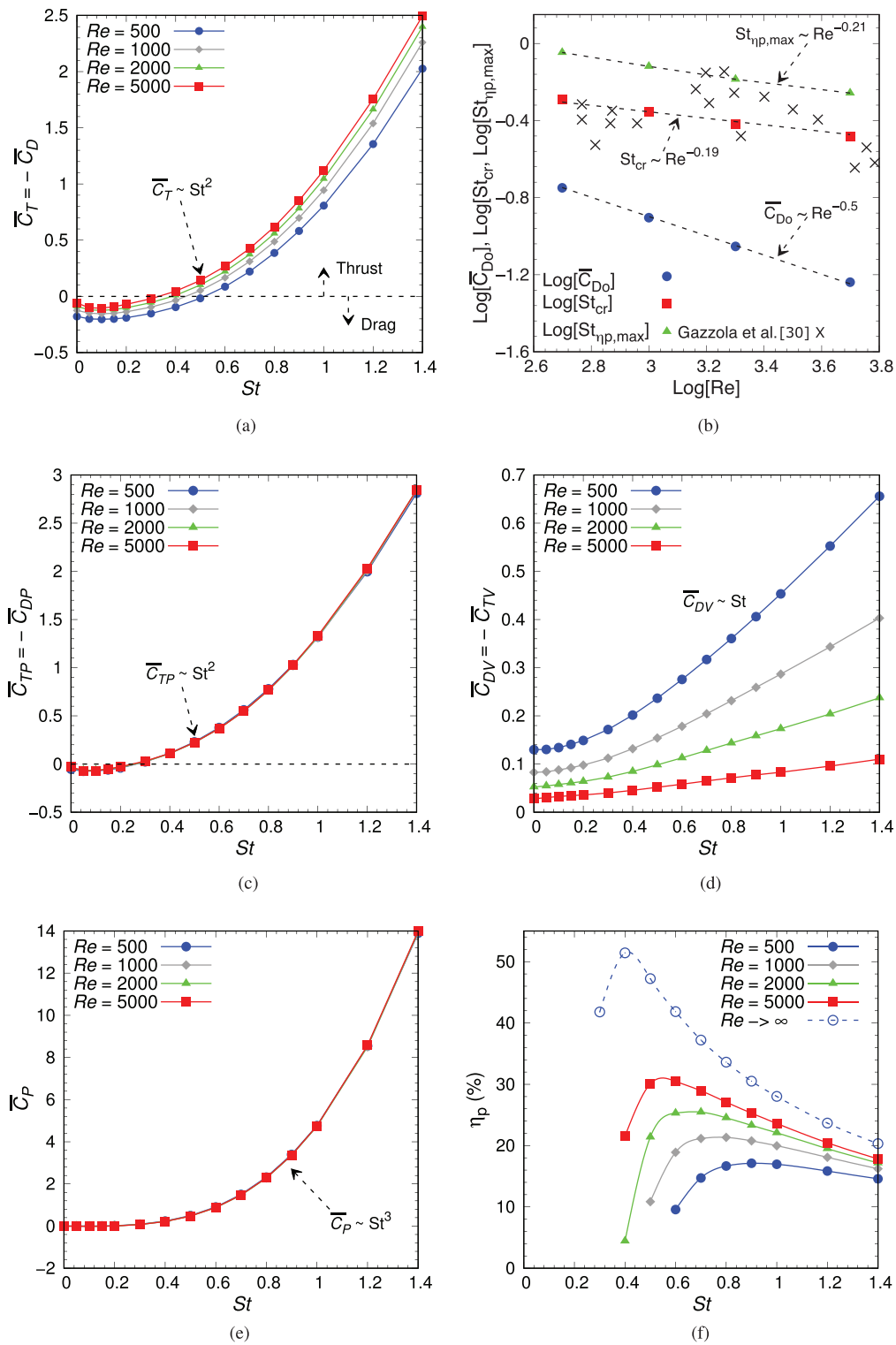


FIG. 4. With increasing non-dimensional frequency St of undulation, variation of time-averaged (a) thrust coefficient \bar{C}_T , (c) pressure thrust coefficient \bar{C}_{TP} , (d) viscous drag coefficient \bar{C}_{DV} , (e) input power coefficient \bar{C}_P , and (f) propulsive efficiency η_p for the various Reynolds numbers examined. (b) shows variation of drag coefficient of a stationary hydrofoil \bar{C}_{D0} , and critical Strouhal number St_{cr} (for that transition from drag to thrust) as a function of Re .

using the arguments outlined by Gazzola *et al.*³⁰ For a unit depth, Gazzola *et al.*³⁰ have shown that the mean pressure thrust (\bar{F}_{TP}) generated by an undulating body scales as $\rho CA_{\max}^2 f^2$. A similar scaling was also derived by Floryan *et al.*³¹ for biologically relevant flapping motions. Thus, the corresponding \bar{C}_{TP} can be scaled as

$$\bar{C}_{TP} = \frac{2\bar{F}_{TP}}{\rho CU_{\infty}^2} = \frac{2\rho CA_{\max}^2 f^2}{\rho CU_{\infty}^2} \sim St^2. \quad (11)$$

Figure 4(d) illustrates the negative value of the second component of \bar{C}_T (\bar{C}_{TV}), the non-dimensional mean viscous drag coefficient ($\bar{C}_{DV} = -\bar{C}_{TV}$), as a function of St for the range of Re considered; note that the drag and thrust coefficients differ by a change in the sign. The figure shows that the viscous drag coefficient \bar{C}_{DV} increases almost linearly with St at high St ($St > 0.2$) and smoothly approaching the viscous drag of a stationary hydrofoil at small St . The rise in \bar{C}_{DV} with St has been well reported in the literature.^{7,32} Further, a linear relationship can also be observed from the results obtained by three-dimensional simulations performed by Borazjani and Sotiropoulos.¹¹

By comparing the curves of Figs. 4(c) and 4(d) at any St , one can observe that the pressure thrust coefficient, \bar{C}_{TP} , is larger than the viscous drag coefficient, \bar{C}_{DV} . Thus, the variation in \bar{C}_T with St behaves much more like \bar{C}_{TP} [shown in Fig. 4(a)], with a quadratic relationship between the two as shown in Fig. 4(c). In the literature, Akbarzadeh and Borazjani³³ derived $\bar{C}_T \sim St^2(1 - 1/V_w^2)$ for a flat plate with a wave traveling along it using elongated body theory while Yu and Huang²⁰ derived $\bar{C}_T \sim St^2(1 - 1/V_w)$ for an undulating hydrofoil using theory based on vorticity dynamics. The difference in scaling is probably due to the difference in the definition of \bar{C}_T since there is no commonly accepted definition for \bar{C}_T and η_p for fish-like undulations.²² However, at large St , $1/V_w \rightarrow 0$ and both the scalings from the literature agree with the present derived scaling.

Figure 4(e) shows the variation of the mean input power coefficient required for undulation, \bar{C}_P , as a function of St for the range of Re considered in this study. Similar to the variation of \bar{C}_{TP} with St , the figure shows that \bar{C}_P also increases with an increase in St . However, \bar{C}_P is independent of Re and the increase in \bar{C}_P with St is cubic in nature, i.e., $\bar{C}_P \sim St^3$, as compared to $\bar{C}_{TP} \sim St^2$. Further, \bar{C}_P variation is non-monotonic with increasing St , where the curve first becomes slightly negative and a crossover from negative to positive occurs close to $St \sim 0.2$ (depending on the Re); seen more clearly below in Fig. 6(c). Interestingly, a similar relationship for \bar{C}_P has also been observed for a pitching hydrofoil by Das *et al.*²⁹ and for a pitching+heaving hydrofoil by Floryan *et al.*³¹ The reason for this cubic relationship can be provided from a scaling analysis similar to that used above for describing the variation in \bar{C}_{TP} . By definition, the input power required for undulation is given as the product of the reaction force exerted by the surrounding fluid (in elementary level) with the local tangential velocity of the foil [Eq. (7)]. Thus, the input power coefficient, \bar{C}_P , can be scaled as:

$$\bar{C}_P = \frac{2\rho CA_{\max}^2 f^2 (A_{\max} f)}{\rho CU_{\infty}^3} \sim St^3. \quad (12)$$

Figure 4(f) illustrates the variation of propulsive efficiency, η_p , as a function of St for the various Re . Note that the efficiency curve contains only those cases that resulted in a net mean thrust. At any St , the figure shows that η_p increases with an increase in Re . The increase in

η_p is due to increasing \bar{C}_T and a constant \bar{C}_P with increasing Re as discussed above, and shown in Figs. 4(a) and 4(e), respectively. It is interesting to observe that the trend of all of these curves, corresponding to different Reynolds numbers, increases initially, attains its maximum value, and then decreases with an increase in St of the foil. Thus for each Re , there is a particular St at which η_p is maximum, which is termed here $St_{\eta_p, \max}$. The variation of $St_{\eta_p, \max}$ with Re is plotted in Fig. 4(b). The figure shows that the $St_{\eta_p, \max}$ varies in the form $St_{\eta_p, \max} = 3.28Re^{-0.21}$, which is very similar to the variation of St_{cr} with Re .

The reason for the increasing–decreasing trend for the efficiency curves can be explained by referring to the \bar{C}_T and \bar{C}_P curves in Figs. 4(a) and 4(e), respectively. Whilst at higher Strouhal numbers the thrust and power coefficients vary approximately as St^2 and St^3 , at lower Strouhal numbers, the thrust coefficient becomes negative, as discussed by Floryan *et al.*³¹ Since, by definition, the propulsive efficiency is the ratio of these two time-averaged quantities, the η_p curve will display the characteristic St^{-1} dependence at high St , but drops away at low St , giving the characteristic peaked efficiency curves. Interestingly, the fall in η_p after attaining a maximum at $St_{\eta_p, \max}$ is intricately associated with asymmetry of the wake and is discussed later in Sec. VI A.

It is interesting to observe that the scalings for the pressure thrust coefficient \bar{C}_{TP} and power coefficient \bar{C}_P for body undulation, presented here for the first time, matches very well with the scalings for a pitching foil provided by Das *et al.*²⁹ However, scalings for other crucial parameters, for instance, St_{cr} , $St_{\eta_p, \max}$, do not match. The similarity in scalings is probably due to the carangiform-like kinematics used in the study by which most of the lateral movements occurs toward the posterior 1/3 of the hydrofoil, as seen in Fig. 1(b). These posterior parts generate most of the pressure thrust and consume power and can be approximated as an oscillating hydrofoil—a more general class of pitching foils, and shown in Fig. 5(d). The difference in scalings of other parameters is due to the anterior 2/3rd part, which undulates like a backward-traveling wave and allows a smoother transfer of momentum between the fluid and the hydrofoil, while also restricting tail motion. Thus, for the present range of Re , body undulations are more efficient than the pure pitching mechanism at high St , as shown in Fig. 5(a). However, less time-averaged net thrust \bar{C}_T is generated for a given Re and St , especially beyond $St = 0.4$, where a sudden enhancement in \bar{C}_T is observed for the rigid pitching foil, as shown in Fig. 5(b). This results in different St_{cr} and $St_{\eta_p, \max}$ variations. A more detailed comparison of the two mechanisms is presented in Thekkethil *et al.*⁶

The propulsion efficiency of a pitching mechanism can be increased by adding heave.³⁴ Indeed, the larger is the heave magnitude, the larger is the enhancement in the propulsive efficiency.³⁴ Thus, in Fig. 5(c), the propulsive efficiency for the present body undulation mechanism is compared with the experimental results of Buren *et al.*³⁴ for an oscillating mechanism (also known as coupled pitching-and-heaving mechanism), heaving at different heave amplitude ho . Note that the results for body undulations are for $Re = 8000$, which is done separately to match with the Re used by Buren *et al.*³⁴ Furthermore, according to the definition of carangiform-like kinematics,³ if we consider the posterior 1/3 part of the hydrofoil as the tail [refer Fig. 5(d)], then according to eq. 5, the maximum lateral displacement of the pivot point of this assumed tail will be $ho = 0.11C'$ (taking

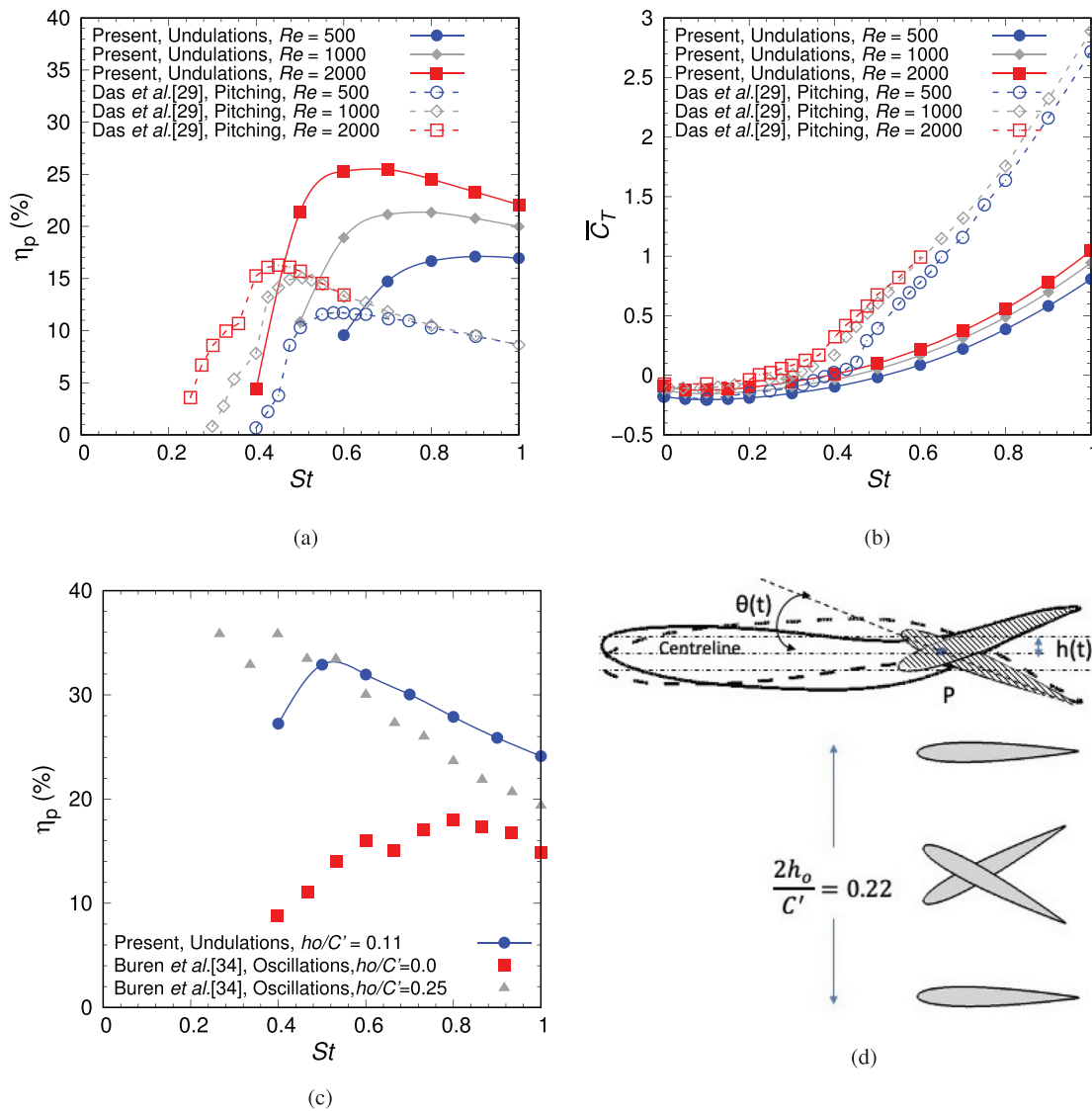


FIG. 5. Comparison of the (a) propulsive efficiency η_p and (b) time-averaged thrust coefficient \bar{C}_T of the present undulating hydrofoil (solid lines) with numerical results provided by Das *et al.*²⁹ for a pitching hydrofoil (dashed lines), pitching at $\theta_{max} = 5^\circ$ and different Re ; (c) propulsive efficiency of the present undulating hydrofoil at $Re = 5000$ with experimental results provided by Buren *et al.*³⁴ for an oscillating hydrofoil at $Re = 8000$, $\theta_{max} = 15^\circ$, and different heave amplitudes; (d) Schematic diagram showing how the posterior 1/3 part of an undulating hydrofoil/body can be approximated as an oscillating hydrofoil.

$C' = 0.33C$ as the chord-length of the assumed tail). Further, it is pitching with $\theta_{max} \sim 11^\circ$ and the phase difference between heave and pitch is 90° . Thus, the maximum lateral displacement of the assumed imaginary tail of body undulations is within the two extreme heave amplitude considered for comparison here (of 0 and 0.25). Figure 5(c) shows that the propulsive efficiency is higher for the undulation mechanism than for the oscillating rigid-foil mechanism ($ho/C' = 0$) for any St . One of the possible reasons for this higher efficiency can be associated with the effective lateral or heaving movement of the assumed tail tip of $ho/C' \sim 0.11$, which is higher than for a purely pitching rigid foil with $ho/C' = 0$. However, if we compare the

efficiency with the oscillating case for $ho/C' = 0.25$, the propulsive efficiency of body undulations are still higher for $St \geq St_{\eta_p, max}$, despite having an effectively much lower heaving amplitude. Thus, this crude comparison hints that the body undulation mechanism is more efficient than the oscillating mechanism for a rigid foil. Of course, a detailed comparison requires further non-dimensional parameters to be considered, for instance, how heave is added to the pitch (sinusoidal or not), the maximum angle of attack and the phase difference between heave and pitch, as these parameters significantly affect the propulsive efficiency.^{35,36} This requires a separate study and is intended for the future.

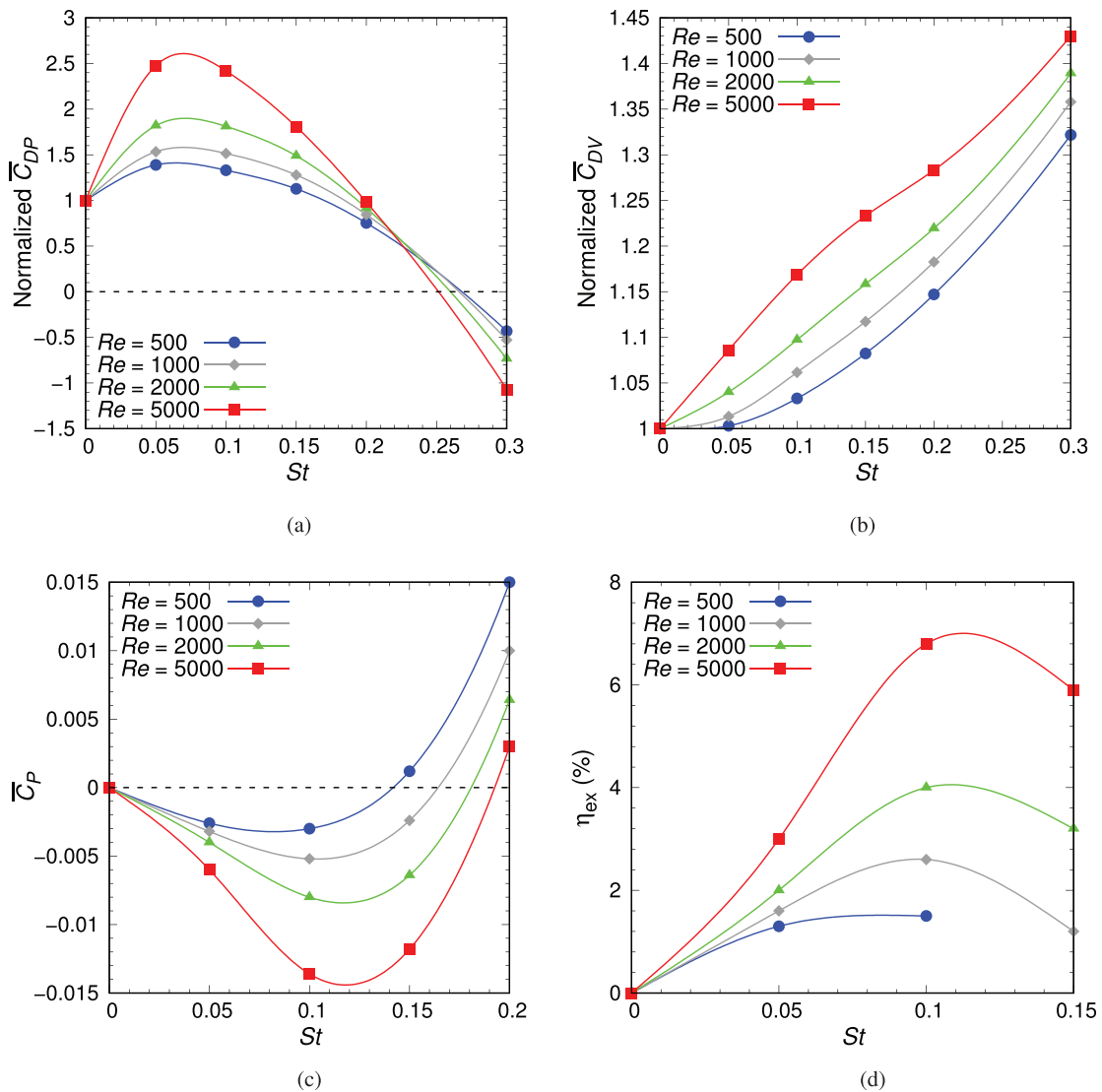


FIG. 6. Variation of time-averaged (a) normalized pressure coefficient \bar{C}_{DP} , (b) normalized viscous coefficient \bar{C}_{DV} , (c) input power coefficient \bar{C}_P , and (d) energy extraction efficiency η_{ex} , with increasing St for various Re . The normalization in (a) and (b) is done by using force coefficients of a stationary hydrofoil at the same Re .

IV. TIME-MEAN ENGINEERING PARAMETERS FOR A NACA0012 HYDROFOIL UNDULATING WITH NON-DIMENSIONAL WAVE-SPEED $V_w < 1$

In Sec. III, Fig. 4(a) shows an increase in drag acting on an undulating hydrofoil compared to a stationary hydrofoil while undulating at $0 < St < 0.2$. These cases are associated with undulations with the non-dimensional wave-speed $V_w < 1$. The higher magnitude of drag for these cases is also reported in the literature as it was observed in two 3-D numerical studies performed by Borazjani and Sotiropoulos^{11,12} for the flow around a carangiform fish-like body undulating at $\lambda^* = 0.95$ at $St = 0.1$, and flow around an anguilliform fish-like body undulating at $\lambda^* = 0.642$ at $St = 0.2$, for two Reynolds numbers of $Re = 500$ and 4000 . In the present section, a more detailed investigation is undertaken showing the significance of non-

dimensional governing parameters, St (in steps of 0.05) and Re (500 – 5000), along with a discussion on the physical mechanism responsible for the drag enhancement. Note the discussion here involves breaking the total drag \bar{C}_D into its pressure (\bar{C}_{DP}) and viscous (\bar{C}_{DV}) components, coupled with the corresponding time-instantaneous vortex structures in the vicinity of the hydrofoil. Further, normalized values of \bar{C}_{DP} and \bar{C}_{DV} , normalized by the corresponding values for a stationary hydrofoil at the same Re , help facilitate the discussion as it ensures easy comparison. The discussion initially focuses on the effect of non-dimensional wave speed V_w on the coefficient of input power consumption \bar{C}_P .

Figure 6(a) shows the variation of the normalized \bar{C}_{DP} with increasing St , for various Re . The corresponding variation of vortex structure in the vicinity of the foil over the range $0.05 \leq St \leq 0.2$ and

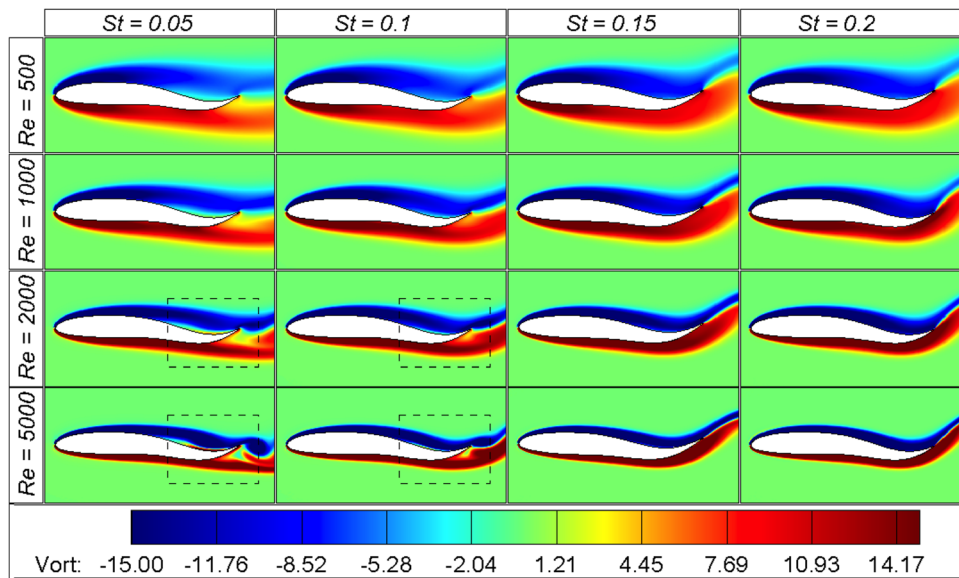


FIG. 7. Instantaneous vorticity contours in the vicinity of the hydrofoil undulating at $St \leq 0.2$ for various Re .

for various Re is shown in Fig. 7. Considering first the undulation motion at a very low frequency of $St = 0.05$, Fig. 6(a) shows a sudden jump in the magnitude of normalized \bar{C}_{DP} . At $St = 0.05$, the hydrofoil is undulating with a wave speed $V_w = 0.25$. Thus, the hydrofoil acts to decelerate the surrounding flow while performing its undulating motion, which in turn leads to flow separation in the trough region of the foil, as shown marked by a rectangular region within which an opposite sign secondary vortex is seen in Fig. 7 at $St = 0.05$. The separated region near the trailing edge of the hydrofoil, corresponds to a low pressure region and thus, enhances the magnitude of pressure drag. As the undulation frequency St increases, the difference between the wave speed and the surrounding free-stream velocity decreases. This decrement in the difference of velocities reduces the severity of flow separation, as shown by a decrease in the size of the secondary vortex in Fig. 7 for $St > 0.05$. The corresponding effect can also be observed in the engineering parameters, as the normalized \bar{C}_{DP} in Fig. 6(a) reduces with an increase in $St (> 0.05)$ of the undulations. With further increase in St to a value matching or exceeding 0.2, the wave speed of undulation becomes either equal to or greater than the surrounding free-stream velocity. Thus, the foil no longer acts to decelerate the surrounding free-stream and the flow remains attached along the chord of the undulating hydrofoil, as shown in Fig. 7 at $St = 0.2$. With attached flow maintained, the adverse pressure gradient vanishes, and thus, Fig. 6(a) at $St = 0.15 - 0.2$ shows that the net pressure drag acting on an undulating hydrofoil becomes almost equal to that of a stationary hydrofoil in a free-stream flow for the various Re examined. The present results on flow separation are consistent with the experimental results provided by Taneda and Tomonari³⁷ for an undulating plate.

Figure 6(a) also shows the effect of Re on normalized \bar{C}_{DP} . For any $St < 0.2$, the figure shows that the magnitude of normalized \bar{C}_{DP} increases with an increase in Re . For instance, at $St = 0.1$, Fig. 6(a)

shows that the enhancement of normalized \bar{C}_{DP} is almost negligible for $Re = 500$, and it increases to almost 2.5 times its value as Re is increased to 5,000. The increase in magnitude is due to the severity of flow separation, which increases with an increase in Re , as shown marked in the contour plots of Fig. 7 at $St = 0.05$. The figure shows that the flow separation is negligible for $Re \leq 1000$, which demonstrates the dominance of viscous forces leading to unseparated flows. However, the figure shows that the flow is separated from the posterior 1/3 of the hydrofoil for higher Re ($Re \geq 2000$). The increase in severity of separation is due to the transition of the flow, from the viscous to inertial regime, with increasing Re . Note that the lateral movements are larger in the posterior 1/3 of the hydrofoil for the carangiform fish-like undulation; refer to Fig. 1(b).

Figure 6(b) illustrates the variation of normalized \bar{C}_{DV} with St for various Re . The figure shows that the flow separation does not significantly affect the time-averaged viscous coefficient, irrespective of the Re . Thus, we can conclude that the increase in total drag \bar{C}_D for cases undulating at $0 < St < 0.2$ is only due to increased pressure drag (\bar{C}_{DP}).

Figure 6(c) depicts the variation of the mean input power coefficient required for undulation, \bar{C}_p , as a function of St for different Re . The figure shows that \bar{C}_p becomes negative for those cases in which the flow gets separated from the hydrofoil ($0.05 \leq St \leq 0.15$). Note from Fig. 6(c) that the negative value of the cycle-averaged input power coefficient \bar{C}_p indicates an output power, which can be extracted by a transmission mechanism similar to that reported for an oscillating mechanism by Kinsey and Dumas.³⁸ The energy is extracted, even with a prescribed motion of the hydrofoil, due to surrounding flow-based favorable phase-difference between the instantaneous C_L and V_{body} [refer Eq. (7) for C_p]. Hence, the present study also shows that the undulation mechanism possesses the potential for harvesting energy from the free-stream as reported by other

researchers,^{14–17} and help elucidate the underlying flow physics. Further analysis is undertaken in Sec. V to reveal more details of this mechanism.

Figure 6(c) also shows the effect of non-dimensional governing parameters, St and Re , on the power-harvesting capabilities of the hydrofoil. With increasing St , the figure shows a decreasing-to-increasing trend, with a minimum near $St = 0.1$, for \bar{C}_P . Further, at any St , the magnitude of \bar{C}_P decreases with an increase in Re . The decrement in the magnitude of \bar{C}_P is a result of increasing severity of flow separation with increasing Re , as discussed above.

Figure 6(d) shows the variation of energy extraction efficiency, η_{ex} [Eq. (8)], as a function of St for the various Re . The figure shows that the η_{ex} increases with increasing St , reaching its maximum at $St = 0.1$, and then decreases eventually. The trend is irrespective of the Re . However, at any St , the energy extraction efficiency increases significantly with an increase in Re . The variation trend of η_{ex} with St and Re is expected as we have observed and discussed above that the minimum C_P occurs at $St = 0.1$, and the severity of flow separation increases with Re .

The highest energy extraction efficiency observed in the present investigation is 6.8%, which is less than the extraction efficiencies from other mechanisms. For instance, Kinsey and Dumas³⁸ observed a maximum extraction efficiency of 34% for an oscillating foil at $ho/C = 1$ and $Re = 1100$. Also, refer to Tables A1 and A2 of Young *et al.*,²⁴ which shows maximum energy extraction efficiencies observed by different research for an oscillating mechanism at different governing parameters. Soti *et al.*³⁹ observed a maximum extraction efficiency close to 30% with a vortex-induced vibration of a circular cylinder oscillating with a maximum amplitude of 0.6 at $Re \sim 5000$. However, it is important to notice here that the kinematics of undulations used for the present simulations are of a carangiform fish, which they developed for efficient propulsion. Further, the swept volume of the surrounding fluid, associated with the maximum lateral displacement of the foil, is significantly lower in the present case than the above discussed oscillating foils and cylinders subjected to VIV. Thus, a different amplitude equation, wavelength, and higher maximum amplitude may result in a comparable extraction efficiency or even better. This is evident as Huang *et al.*¹⁴ observed an increase in extraction efficiency of undulations mechanism from 5% to 26.92% while increasing A_{max} from 0.1 to 0.4 at $Re = 5000$.

V. BODY UNDULATIONS—FROM POWER CONSUMING TO POWER HARVESTING?

Sections III and IV show that the undulation mechanism is a thrust generating mechanism that consumes power for undulation at $St > 0.2$. In contrast, it changes to a power harvesting mechanism in which a high drag acts on the hydrofoil while undulating at $St < 0.2$. To understand this switch, a detailed analysis is performed for two cases: (i) $St = 0.4$, with $V_w > 1$ corresponding to positive power consumption with a net positive output thrust force; and (ii) $St = 0.1$, with non-dimensional wave speed $V_w < 1$ corresponding to negative input power and a net negative (drag) output force. The study is performed using time-varying instantaneous pressure and vorticity contours correlated with the input power coefficient (C_P) variation over an undulation cycle, as shown in Fig. 8.

As a thrust-generation mechanism, body undulations are associated with a backward-traveling wave, resulting in backward traveling crest and trough regions propagating along the chord length. These

traveling crest and trough regions push and suck the surrounding fluid, respectively, creating positive and negative pressures across the body that provide the required thrust force for propulsion. Thus, the mechanism is known as the *pressure-suction* mechanism.⁴⁰ This is re-studied here, along with an addition of time-instantaneous power consumption of the hydrofoil undulating at $St = 0.4$ in panels 8(a₁)–8(f₂) and 8(g). Panels 8(b₁) and 8(b₂) show that the onset of the motion from the mean position occurs with the leftward motion of the tail tip. This hydrofoil movement creates a local crest in the rightward side, pushing the surrounding fluid and building a local positive region. In contrast, the movement create a local trough region in the hydrofoil's leftward side that sucks the surrounding fluid toward it and builds a local negative pressure region. Thus, a net normal force acts on the hydrofoil from the fluid in the direction from the positive to negative pressure region, shown as a red vector in the figure, whose streamwise component provides the instantaneous thrust for propulsion. The figure also shows that the hydrofoil is moving against the direction of the reaction force, and thus the instantaneous power consumption of the hydrofoil is positive and increases compared to the mean position, as shown in Fig. 8(g). Further along in undulation phase, the tail tip reaches the leftmost excursion point shifting the crest and trough regions closer to the tail tip. Note that according to Eq. (5), the amplitude of lateral undulation increases quadratically while traveling toward the tail tip. Thus, the size of the crest-and-trough regions are larger closer to the tail tip. These larger sizes push and suck a larger volume of the surrounding fluid, resulting in a larger pressure gradient across the hydrofoil. The larger pressure gradient leads to a larger reaction force and a larger power consumption, as shown in Fig. 8(g). With a further hydrofoil movement, the tail tip starts traveling toward the rightward direction, and the crest and trough regions form closer to the leading edge. At this time in the cycle, the sizes of these regions are comparatively small, leading to the generation of a comparatively smaller reaction force contributions and smaller power consumption. The decreasing trend of power consumption continues until the tail tip reaches the central mean position (d₁); following this point the figure shows that the power consumption again increases as the crest and trough regions travel toward the tail tip. Thus, for the sinusoidal undulating hydrofoil with wave speed larger than the surrounding fluid stream ($V_w > 1$), a sinusoidal positive output thrust (not shown here) is observed together with sinusoidal positive input power consumption, as shown in Fig. 8(g).

For $St = 0.1$, panels 8(a₃)–8(f₃) show similar body movements to those for $St = 0.4$, though in this case, the wave speed of undulations is less than the surrounding fluid flow velocity, i.e., $V_w < 1$. This lesser wave speed results in the flow separation and can be seen along the hydrofoil crest regions in the magnified vortex contours of panels 8(a₄)–8(f₄). Further, notice that such flow separation contrasts to the hydrofoil throughout the cycle, as shown in magnified vortex contours of Figs. 8(a₂)–8(f₂). This flow separation alters the fluid condition around the hydrofoil undulating at $St = 0.1$ such that panels 8(a₃)–8(f₃) show an intensive negative pressure zone along the crest regions of the hydrofoil throughout the cycle. Thus, the fluid exerts a normal reaction force in the opposite direction than $St = 0.4$, whose streamwise component results in high drag. In addition, notice from the contour plots of panels Figs. 8(a₃)–8(f₃) that the hydrofoil moves in the direction of the fluid force. Thus, the surrounding fluid assists in the

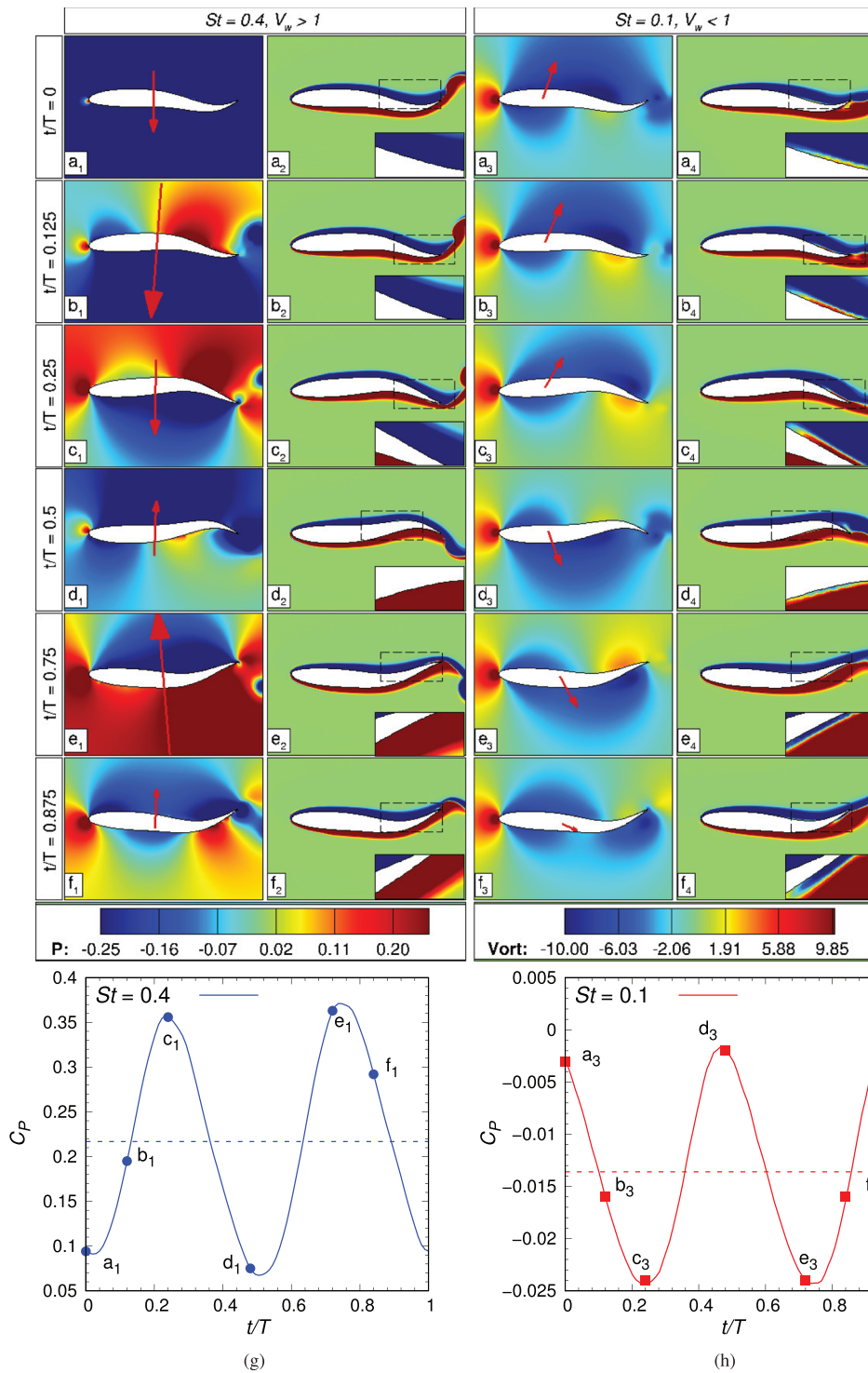


FIG. 8. Study examining the temporal variation in the instantaneous pressure and vorticity contour along with instantaneous power coefficient C_p for a hydrofoil undulating with $(a_1)-(f_2)$ and (g) $St=0.4$ and $(a_3)-(f_4)$ and (h) $St=0.1$ at $Re=5000$. The red arrows in pressure contours $(a_1)-(f_1)$ and $(a_3)-(f_3)$ represent the vector plot for the net force acting on the hydrofoil. The bottom right region in the vortex contours $(a_2)-(f_2)$ and $(a_4)-(f_4)$ represents the zoomed vortex contours within the marked rectangular region of the corresponding frame.

hydrofoil's motion, resulting in a negative power coefficient (or harvesting of energy from the fluid flow) at any time instant of the cycle, as shown in the line plot for time-instantaneous power coefficient (C_p) in Fig. 8(h). Thus the reason behind the sinusoidal increase or decrease

in power consumption/harvesting is similar to that for $St=0.4$, as discussed in the previous paragraph.

Thus, the underlying flow physics for body undulations is similar to that governing oscillation of a rigid foil. For a rigid foil undergoing

oscillation, there exists a *feathering parameter* that provides the limit below which the hydrofoil/body generates thrust, and above it, the hydrofoil/body extracts energy from the surrounding fluid flow.³⁸ Similarly, for body undulation, there exists a non-dimensional parameter V_w that gives the necessary, but not precisely sufficient, condition for differentiating power harvesting and thrust generating capabilities, such that $V_w < 1$ is associated with power harvesting/extraction, whereas $V_w > 1$ corresponds to positive pressure thrust generated by the body.

VI. INSTANTANEOUS WAKE-PATTERN-BASED FLOW REGIMES

Fluid-structure interaction can often lead to the formation of vortices, as a result of vorticity generation at the surface of the structure, which can be associated with a momentum transfer between the fluid and structure/body.⁴¹ Quantification of these vortices can be very helpful for understanding the current problem of an undulating hydrofoil at different St and Re . This section documents and discusses the various wake structures observed in this broad parametric investigation.

A. Wake regime map

A change in St of undulation and Re of the flow brings systematic changes to the wake of an undulating body. The changes include qualitatively different wake patterns, which can be characterized by the arrangement of shed vortices and the overall wake inclination with the free-stream.

Figure 9(a) presents a regime map of the different wake patterns, corresponding to the various St and Re . The wake structures are shown as instantaneous vorticity and time-averaged streamwise velocity contour plots in panels 9(b)–9(i). Note that the wake patterns are categorized based on an analysis of the instantaneous vorticity contours within five chord lengths downstream of the hydrofoil; however, in some cases the wake may further evolve to present different characteristics further downstream.

For a stationary hydrofoil, i.e., $St = 0$, the wake regime map [refer to Fig. 9(a)] indicates a steady wake behind the hydrofoil, and the wake topology is independent of Reynolds number. The corresponding wake structure is shown in Fig. 9(b), which shows a steady flow with two opposite-sign shear layers attached to the hydrofoil and no vortex shedding. With the start of lateral undulation of the hydrofoil at $St = 0.05$, Fig. 9(a) shows the first transition observed in the study and also the significance of Re on the flow separation (as discussed in Sec. IV). For $Re \leq 1000$, transition occurs to a wavy wake. The characteristics are shown in Fig. 9(c), which show attached wavy shear layers in the hydrofoil wake without formation of discrete vortex structures. In contrast, for $Re \geq 2000$, transition occurs to a dipole-based vortex street. Figure 9(d) shows that the wake characteristics include flow separation, leading to shedding of two dipoles/couplets during each cycle of undulation. Thus, the severity of flow separation at low St , discussed in Sec. IV, also affects the wake structure behind an undulating hydrofoil. With an increase in undulation frequency to $St = 0.1$, the significance of the flow separation reduces slightly, and the wake regime map for $St = 0.1$ shows a transition to the stretched vortex-based vortex street behind the foil; refer to Fig. 9(e). The figure shows a stretched alternate-signed vortex street, in which the center of clockwise (CW) and counterclockwise (CCW) vortices lie below and above the

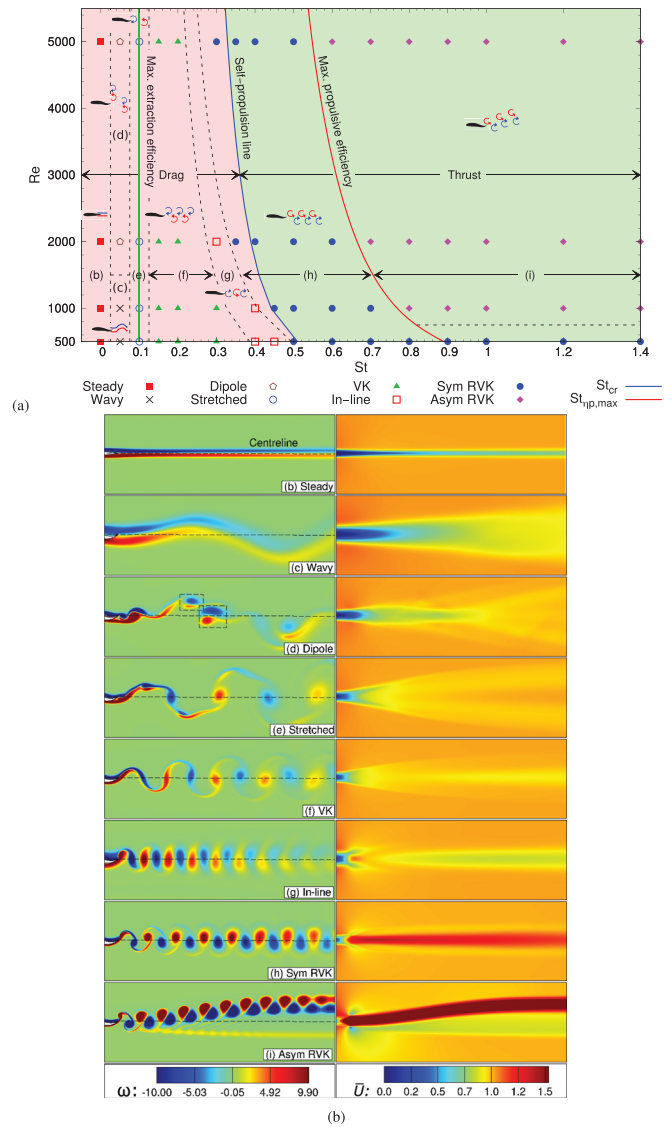


FIG. 9. (a) Wake regime map in the St – Re parameter space, representing the eight different wake modes associated with an undulating hydrofoil, (b)–(i) instantaneous vorticity and time-averaged streamwise velocity contours for $Re = 5000$, at a St equal to (b) 0, (d) 0.05, (e) 0.1, (f) 0.2, (h) 0.4, (i) 0.8; $Re = 500$ at a St equal to (c) 0.05, (g) 0.4. Here, the vortex streets are represented as VK: von-Karman; RVK: reverse von-Karman; and Asym: asymmetric. For (a) the dashed line demarcates the St – Re boundary for the mean drag to mean thrust generation by the hydrofoil. The dashed-dotted line represents demarcation for the symmetric and asymmetric wake patterns in the map. Note that the dashed-line corresponds to the curve fitted results for the critical Strouhal number St_{cr} , while the dashed-dotted line is an approximate representation of the boundary.

centerline passing through the center of the foil (shown as a dashed line). Furthermore, this wake pattern is found to be independent of Re , as seen in Fig. 9(a) at $St = 0.1$. With a further increase to $St = 0.15$, the difference between wave speed and surrounding free-stream velocity reduces ($V_w = 0.75$), which diminishes the effect of flow separation

and leads to the formation of a characteristic von-Karman (VK) vortex street as shown in Fig. 9(f). The figure shows the VK street as a set of alternate-signed vortices, with centers of the CW and CCW vortices situated above and below the line passing through the streamwise centerline of the foil, respectively. This arrangement of vortices induces the surrounding flow in the stream-wise direction, which leads to the production of a stream-wise *momentum-deficit wake*, as shown in time-averaged streamwise velocity contour of Fig. 9(f). A similar vortex street has been observed by Dong and Lu¹⁰ for an undulating NACA0012 hydrofoil at $St = 0.16$ and $Re = 5000$.

The wave speed of undulation becomes greater than the free stream velocity at $St = 0.3$, and the wake regime map in Fig. 9(a) shows two different transitions in the wake, depending on Re . It can be seen that the first transition is from a VK to an in-line vortex street at $Re = 2000$; and the second transition is from the in-line to a reverse von-Karman (RVK) vortex street at $Re = 5000$. The in-line vortex street is shown in Fig. 9(g), with the centers of the CCW and CW vortices residing almost along the centerline of the foil. This arrangement of vortices does not induce the surrounding flow, and thus, results in a stream-wise *momentum-less wake*, as shown in time-averaged streamwise velocity contour of Fig. 9(g). The characteristics of the RVK vortex street are contrary to that of a VK vortex street as seen in Figs. 9(f) and 9(h). For an RVK street, Fig. 9(h) shows that the centers of the CW and CCW vortices lie below and above the line passing through the center of the foil, respectively. Thus, the vortices induce the surrounding flow opposite to the streamwise direction and generate a *momentum-excess jet* behind the foil (thus leading to thrust), as shown in time-averaged streamwise velocity contour of Fig. 9(h). For $Re \leq 1000$, Fig. 9(a) shows that the transition from the VK street first occurs to an in-line vortex street at $St = 0.4$, followed by the transition to an RVK vortex street at $St = 0.45$ for $Re = 1000$ and $St = 0.5$ for $Re = 500$; the respective transition occurs at a smaller $St = 0.3$ and 0.35 for the larger $Re = 2000$. Thus, as might be expected, the critical St for the onset of an in-line and RVK vortex street decreases with an increase in Re .

At $St = 0.6$, Fig. 9(a) shows a transition from a symmetric RVK to asymmetric RVK vortex street for the higher Reynolds number of $Re = 5000$. The asymmetric RVK vortex street is shown in Fig. 9(i), where one can notice that the vortices move toward the rightward lateral direction (refer to Fig. 2 for the definition of the right side) that leads to the asymmetry of the wake. A detailed analysis of this flow behavior is presented in Sec. VIB. For $Re = 2000$, asymmetry in the RVK street is observed in Fig. 9(a) at $St \geq 0.7$, whereas it is observed at $St \geq 0.8$ for $Re = 1000$. It is interesting to observe from the regime map that the asymmetric wake structure is not generated at the smallest simulated value of $Re = 500$, even for the maximum value of St simulated here. This is due to dominant viscous forces, which reduce the required local induced velocity for the deviation. Please note that the asymmetric wakes are not common in nature since the operating range of St for fish-swimming is low ($St = 0.25 - 0.35$).¹⁸ Further, in order to check the possible effect of domain size on asymmetry observed here, a simulation for $St = 0.8$ and $Re = 5000$ (case in which we observed the maximum asymmetry of vortex street, discussed in Sec. VIB) was done on a 25% larger domain (in the lateral direction). The asymmetry in the flow was still observed, and almost the same results were obtained. A detailed discussion of the cause of the wake deflection and its dependence on governing parameters and initial conditions is given in Sec. VIB.

The wake regime map in Fig. 9(a) also presents the $St_{np,max}$ curve that almost coincides with the symmetric RVK to asymmetric RVK transition—indicating the link between flow transition and the decreasing observed propulsive efficiency of body undulations above $St_{np,max}$. The reduced efficiency with the development of an asymmetric wake can be explained by considering the streamwise and lateral components of the net time-averaged normal reaction force acting on the hydrofoil. For an asymmetric wake, the time-averaged lateral component is not zero and results in a small mean lift. Thus, in effect, this part of the reaction force is lost and not converted into a mean thrust, leading to reduced propulsive efficiency. The wake regime map also shows that the transition of the wake from the VK to RVK vortex street does not always occur exactly at the drag to thrust transition. Similar findings are reported by Godoy-Diana *et al.*,⁴² Das *et al.*,²⁹ and Chao *et al.*⁴³ for a pitching rigid hydrofoil. In particular, for body undulations, the transition first occurs to an in-line vortex street for $Re \leq 2000$, whereas it occurs directly to a reverse von-Karman street for $Re = 5000$.

B. Asymmetric wake

For many of the wake states examined, changes to the non-dimensional governing parameters or initial motion do not significantly affect the wake structures (despite a change in vortex strength and local distance between vortices); however, the same is not true for asymmetric wakes. Thus, the current section addresses the underlying reason for wake asymmetry using time-varying instantaneous vorticity contours, and documents the effect of governing parameters and initial conditions on the asymmetry.

Figure 10 shows the temporal variation of the instantaneous vortical wake structures over the first 40 cycles at $St = 0.8$ and $Re = 5000$. In the figure, the right column displays the zoomed vorticity contours (along with the overlapped velocity vectors) for the rectangular regions marked in the main (left column) contour plots, whereas the left column represents vorticity contours zoomed along the line passing through the center of the hydrofoil, providing a total width of 1.4 C. The figure shows that the undulation motion (discussed here concerning the tail tip) starts with the leftward motion of the tail tip from its mean central position. Notice from the velocity vectors that the hydrofoil motion accelerates the surrounding fluid along with it and a vortex is shed from the tail tip when the direction of its motion changes, after reaching either rightmost or leftmost excursions, shown in Fig. 10 for $n = 0.5$ cycles. Thus, two vortices are shed in one complete cycle of undulations. Note that the frequency of vortex shedding depends on St , whereas the downstream convection of the shed vortices, in the far wake, depends on Re . At large St (for instance $St = 0.8$), the frequency of shed vortices is very large as compared to their convection (frequency) scale. This difference results in the two consecutive shed vortices reaching very close to each other (to form a dipole) after 2 cycles of undulation, as shown in Fig. 10 for $n = 2$ cycles.

Here, the term dipole refers to two opposite-sign vortices that are very close to each other, with mutual induction propelling them along their dipole axis.²⁷ Thus the vortices now travel with a velocity governed by the combined effect of the free-stream and local induction, which leads to the deviation of vortices from the streamwise direction—shown in Fig. 10 for $n = 2.5$ and 3.0. After traveling a certain distance, the figure for $n = 20$ cycles shows that the deviation of vortices in the lateral direction diminishes, and they convect further

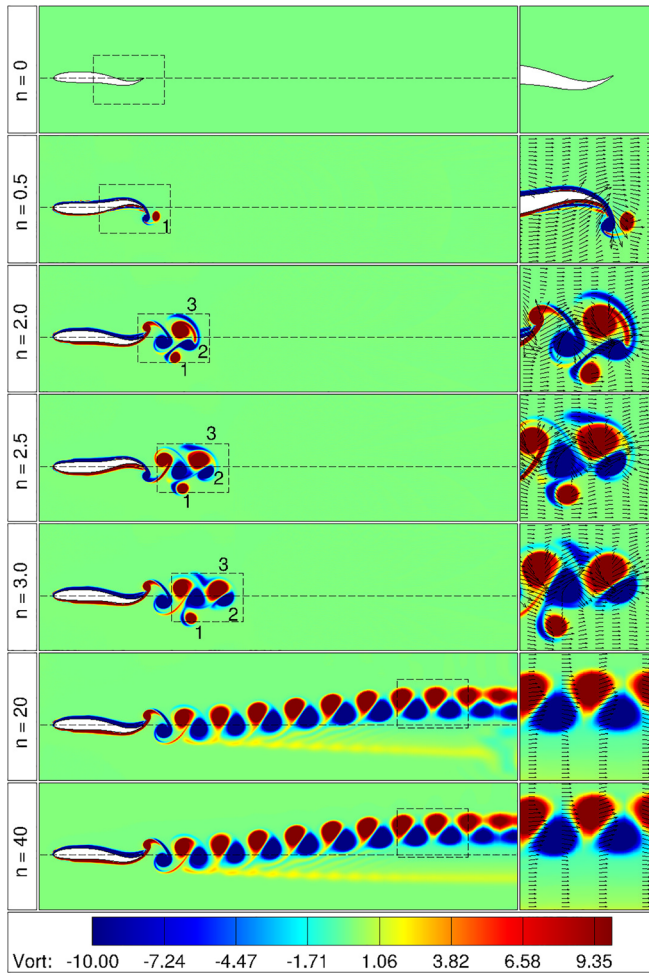


FIG. 10. Temporal variation of instantaneous wake vorticity for the first $n=40$ undulation cycles at $St=0.8$ and $Re=5000$. The right column contour plots illustrate the instantaneous vorticity along with velocity vectors within the marked rectangular region of the left images.

downstream in the streamwise direction. It can be seen that this change corresponds to the downstream diffusing wake developing into a more symmetric set of positive and negative vortices rather than the recognizable set of dipoles seen in the near wake.

The direction of the lateral deviation of the vortex street depends on the relative position of vortices within the dipole. If the arrangement of shed-vortices is such that the CW (CCW) vortex is leading the CCW (CW) vortex, the dipole will cause induction in the rightward (leftward) lateral direction, resulting in the deviation/tilting of the street in the same direction. The relative position of the vortices within the dipole depends upon the direction of the onset of undulation of the hydrofoil; used as an initial condition in the present simulation. Figure 11 shows the vortex street for the two types of onset of undulations of the hydrofoil, with the inclination of the RVK vortex street for the undulation as rightward for the mean-left; and leftward for the mean-right onset of undulations.

The asymmetry in the wake depends on both St and Re . Figures 12(a) and 12(b) show the effect of St and Re on the lateral deviation, ΔY , of the relaminarized vortex street; shown marked in Fig. 11. Figure 12(a) shows that the asymmetric wake is generated for $St \geq 0.6$, and the variation of the magnitude of lateral deviation (ΔY) with increasing St is of the increasing-decreasing type with maximum deviation at $St=0.8$. The trend is due to the increase in shed vortex strength with increasing St , which leads to the larger lateral deviation of the street. However, for $St > 0.8$, the vortices become so strong that they form another dipole with a leading vortex of opposite sign. The newly formed dipole pulls the wake in the opposite direction, resulting in a reduced overall deviation in the far wake. With increasing Re at $St=0.8$, Fig. 12(b) shows an asymptotic increase in ΔY , which is due to the reduction in viscous forces with increasing Re .

VII. CONCLUSIONS

In conclusion, a systematic numerical investigation has been undertaken to evaluate the energetic cost of propulsion for a NACA0012 hydrofoil, undulating with a maximum amplitude of 0.1 over a wide range of Strouhal ($0 \leq St \leq 1.4$) and Reynolds numbers ($500 \leq Re \leq 5000$). The study was carried out by using a level-set function-based immersed interface method (LS-IIM). It was found that the time-averaged thrust exhibited a quadratic variation with St with significant dependence on Re . After splitting the time-averaged thrust into its two components, it was observed that the quadratic variation with St is due to its pressure component, whereas the variation with Re is due to its viscous component. In contrast to this, the time-averaged input power coefficient was found to be independent of Re and increases cubically with St . These observations were shown to be consistent with scaling analysis, which also predicted the observed St variations of thrust and power. The propulsive efficiency calculated by these two time-averaged quantities shows an increasing-and-decreasing trend, which depends significantly on Re . Thus, for each Re , there exists an St at which the propulsive efficiency is maximum, termed $St_{np,max}$. It has been observed here that $St_{np,max}$ decreases with an increase in Re , following the relationship $St_{np,max} = 3.28Re^{-0.21}$. Further, for the present range of Re , the derived scaling for drag to thrust transition St_{cr} lies within the range of actual St found for real fish and birds for their propulsion, as provided by Gazzola *et al.*³⁰

This detailed investigation provides an understanding of the force and power coefficients, and the flow structure in the vicinity of the hydrofoil at very low St —when the wave speed is less than the surrounding free-stream velocity. It is observed that the hydrofoil experiences a greater drag compared to a stationary foil at the same Re . The flow separation is found to be responsible for this enhancement of drag, whose severity is directly proportional to Re and is inversely dependent on St . Furthermore, the time-averaged input power coefficient was observed to be negative in this range of St with a minimum magnitude at $St=0.1$, and decreases with increasing Re . The negative input power coefficients imply that the foil no longer needs a continuous input power to undulate and in fact, can extract/harvest energy from the free-stream. Thus, further investigation is carried out to elucidate how the body-undulation mechanism switches between power-consuming (thrust generating) and power-harvesting, with varying non-dimensional wave speed.

A comprehensive characterization of wake structures has been undertaken by marking the arrangement of shed vortices, inclination with the free-stream, and different structures present especially in the

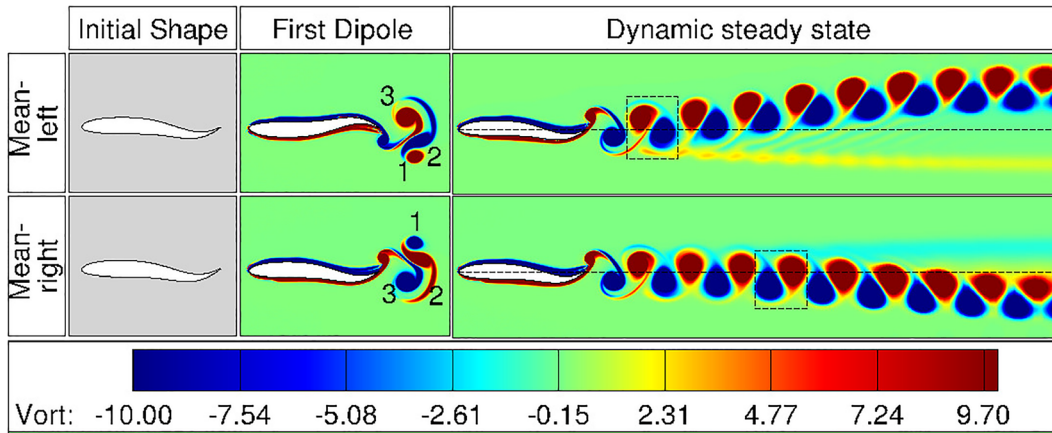


FIG. 11. For the two different types of onset of undulations of the foil in the present simulation, instantaneous vorticity contour after the first dipole formation and the periodic state for $St = 0.8$ and $Re = 5000$.

near-wake. The resulting wake regime map shows eight different wake types that vary with increasing St and Re —from steady symmetric to asymmetric wakes. The map shows that the generation of the asymmetric wake is associated with decreasing propulsive efficiency of body undulations. The wake map also shows that the transition from a von-Karman street to a reverse von-Karman street depends significantly on Re . Notably, for $Re \leq 2000$, the transition first occurs to an in-line vortex street, whereas it occurs directly to a reverse von-Karman for $Re = 5000$. For all values of Re , the transition precedes the transition from a wake having a time-averaged drag to one having a time-averaged thrust generated by the hydrofoil. The asymmetry in the wake arises from the formation of local dipoles within near wake. The direction of lateral deviation depends on the initial movement of the hydrofoil, and the magnitude of deviation shows an increasing-

decreasing trend with increasing St , with a maximum at $St = 0.8$. Further, the deviation increases with increasing Re as downstream viscous diffusion decreases.

Body undulations belong to one of the three bio-inspired underwater propulsion mechanisms derived from BCF fish with application to the development of modern underwater vehicles. The mechanism investigated here is inspired by the body undulations performed by anguilliform and carangiform types of BCF fish. The other two are pitching and oscillating (pitching+heaving) mechanisms that are inspired by the lateral motion of the tail of thunniform fish. It is interesting to note that the three different approximations to BCF fish-like locomotion result in a similar scaling for the pressure thrust and input power coefficient with oscillation frequency. However, by comparing the propulsive efficiency of these three different bio-inspired

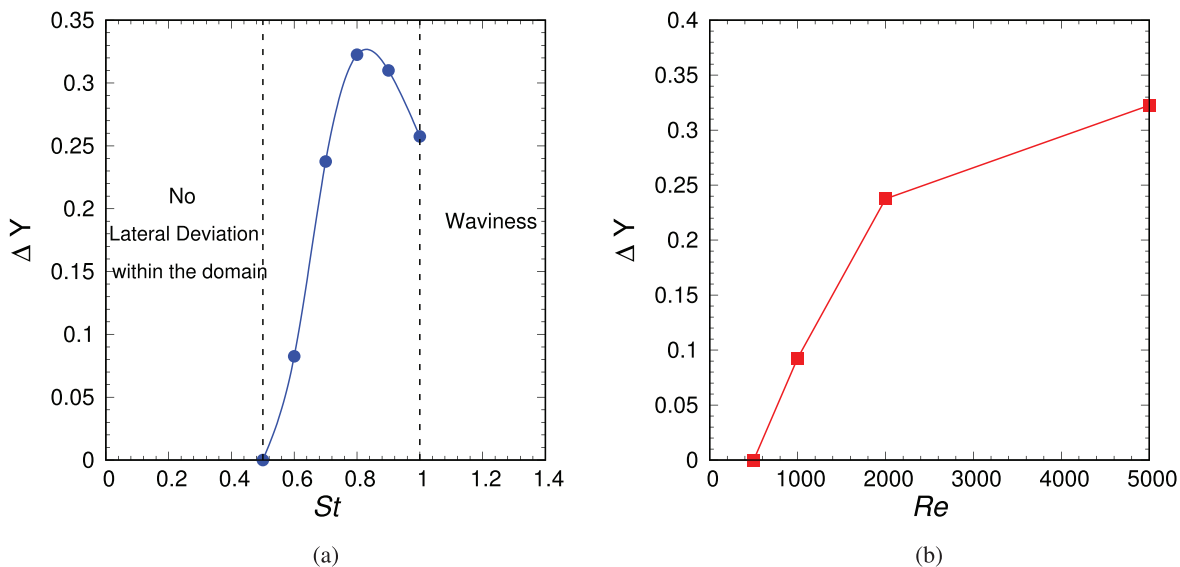


FIG. 12. Lateral deviation in the wake measured from the centerline, with increasing (a) St at $Re = 5000$ and (b) Re at $St = 0.8$.

mechanisms, body undulations appear superior for a similar range of non-dimensional governing parameters. In addition, together with the oscillating mechanism, body undulation also possesses the capability of extracting power from the free stream. Finally, the results and scalings presented in this paper could provide valuable input for the design and development of the modern underwater propulsion systems and energy extraction devices.

ACKNOWLEDGMENTS

The support of a scholarship from the IITB-Monash Research Academy and funding from the Australian Research Council Discovery Grant Nos. DP170100275 and DP190103388 are gratefully acknowledged.

AUTHOR DECLARATIONS

Conflict of Interest

The authors have no conflicts to disclose.

DATA AVAILABILITY

The data that support the findings of this study are available from the corresponding author upon reasonable request.

REFERENCES

- ¹C. M. Breder, "The locomotion of fishes," *Zoologica* **4**, 159–291 (1926).
- ²C. C. Lindsey, "Form, function and locomotory habits in fish," *Fish Physiol.* **7**, 1–100 (1978).
- ³M. Sfakiotakis, D. M. Lane, and J. B. C. Davies, "Review of fish swimming modes for aquatic locomotion," *IEEE J. Oceanic Eng.* **24**, 237–252 (1999).
- ⁴A. P. Maertens, A. Gao, and M. S. Triantafyllou, "Optimal undulatory swimming for a single fish-like body and for a pair of interacting swimmers," *J. Fluid Mech.* **813**, 301–345 (2017).
- ⁵M. Abbaspour and M. Ebrahimi, "Comparative numerical analysis of the flow pattern and performance of a foil in flapping and undulating oscillations," *J. Mar. Sci. Technol.* **20**, 257–277 (2015).
- ⁶N. Thekkethil, A. Sharma, and A. Agrawal, "Unified hydrodynamics study for various types of fishes-like undulating rigid hydrofoil in a free stream flow," *Phys. Fluids* **30**, 077107 (2018).
- ⁷M. J. Lighthill, "Large-amplitude elongated-body theory of fish locomotion," *Proc. R. Soc. London, Ser. B* **179**, 125–138 (1971).
- ⁸H. Liu, R. Wassersug, and K. Kawachi, "A computational fluid dynamics study of tadpole swimming," *J. Exp. Biol.* **199**, 1245–1260 (1996).
- ⁹J. Deng, X. M. Shao, and A. L. Ren, "Numerical study on propulsive performance of fish-like swimming foils," *J. Hydrodyn.* **18**, 681–687 (2006).
- ¹⁰G. J. Dong and X. Y. Lu, "Characteristics of flow over traveling wavy foils in a side-by-side arrangement," *Phys. Fluids* **19**, 057107 (2007).
- ¹¹I. Borazjani and F. Sotiropoulos, "Numerical investigation of the hydrodynamics of carangiform swimming in the transitional and inertial flow regimes," *J. Exp. Biol.* **211**, 1541–1558 (2008).
- ¹²I. Borazjani and F. Sotiropoulos, "Numerical investigation of the hydrodynamics of anguilliform swimming in the transitional and inertial flow regimes," *J. Exp. Biol.* **212**, 576–592 (2009).
- ¹³H. Yu, X.-Y. Lu, and H. Huang, "Collective locomotion of two uncoordinated undulatory self-propelled foils," *Phys. Fluids* **33**, 011904 (2021).
- ¹⁴D. Huang, J. Zhang, and X. Sun, "New method for harvesting energy from fluid flow based on undulatory motion," *Int. J. Green Energy* **14**, 540–547 (2017).
- ¹⁵F. Ji and D. Huang, "Effects of Reynolds number on energy extraction performance of a two dimensional undulatory flexible body," *Ocean Eng.* **142**, 185–193 (2017).
- ¹⁶L. Ding, H. Li, and D. Huang, "Parametric research on energy extraction of a waving plate with unequal amplitude traveling wave motion," *Energy Sources, Part A* **42**, 2063–2081 (2020).
- ¹⁷X. Sun, F. Ji, S. Zhong, and D. Huang, "Numerical study of an undulatory airfoil with different leading edge shape in power-extraction regime and propulsive regime," *Renewable Energy* **146**, 986–996 (2020).
- ¹⁸G. S. Triantafyllou, M. S. Triantafyllou, and M. A. Grosenbaugh, "Optimal thrust development in oscillating foils with application to fish propulsion," *J. Fluids Struct.* **7**, 205–224 (1993).
- ¹⁹M. Ragheb and A. M. Ragheb, "Wind turbines theory-the betz equation and optimal rotor tip speed ratio," *Fundam. Adv. Top. Wind Power* **1**, 19–38 (2011).
- ²⁰Y.-L. Yu and K.-J. Huang, "Scaling law of fish undulatory propulsion," *Phys. Fluids* **33**, 061905 (2021).
- ²¹J. J. Videler and F. Hess, "Fast continuous swimming of two pelagic predators, saithe (*Pollachius virens*) and mackerel (*Scomber scombrus*): A kinematic analysis," *J. Exp. Biol.* **109**, 209–228 (1984).
- ²²A. Maertens, M. S. Triantafyllou, and D. K. Yue, "Efficiency of fish propulsion," *Bioinspiration Biomimetics* **10**, 046013 (2015).
- ²³Y. Pan and H. Dong, "Computational analysis of hydrodynamic interactions in a high-density fish school," *Phys. Fluids* **32**, 121901 (2020).
- ²⁴J. Young, J. C. Lai, and M. F. Platzer, "A review of progress and challenges in flapping foil power generation," *Prog. Aerosp. Sci.* **67**, 2–28 (2014).
- ²⁵C.-L. Yu, Y.-H. Hsu, and J.-T. Yang, "The dependence of propulsive performance on the slip number in an undulatory swimming fish," *Ocean Eng.* **70**, 51–60 (2013).
- ²⁶N. Thekkethil and A. Sharma, "Level set function-based immersed interface method and benchmark solutions for fluid flexible-structure interaction," *Int. J. Numer. Methods Fluids* **91**, 134–157 (2019).
- ²⁷N. Thekkethil, A. Sharma, and A. Agrawal, "Self-propulsion of fishes-like undulating hydrofoil: A unified kinematics based unsteady hydrodynamics study," *J. Fluids Struct.* **93**, 102875 (2020).
- ²⁸N. Thekkethil, A. Sharma, and A. Agrawal, "Three-dimensional biological hydrodynamics study on various types of batoid fishlike locomotion," *Phys. Rev. Fluids* **5**, 023101 (2020).
- ²⁹A. Das, R. Shukla, and R. N. Govardhan, "Existence of a sharp transition in the peak propulsive efficiency of a low Re pitching foil," *J. Fluid Mech.* **800**, 307–326 (2016).
- ³⁰M. Gazzola, M. Argentina, and L. Mahadevan, "Scaling macroscopic aquatic locomotion," *Nat. Phys.* **10**, 758 (2014).
- ³¹D. Floryan, T. Van Buren, and A. J. Smits, "Efficient cruising for swimming and flying animals is dictated by fluid drag," *Proc. Natl. Acad. Sci. U. S. A.* **115**, 8116–8118 (2018).
- ³²E. J. Anderson, W. R. Mcgillis, and M. A. Grosenbaugh, "The boundary layer of swimming fish," *J. Exp. Biol.* **204**, 81–102 (2001).
- ³³A. Akbarzadeh and I. Borazjani, "Reducing flow separation of an inclined plate via travelling waves," *J. Fluid Mech.* **880**, 831–863 (2019).
- ³⁴T. V. Buren, D. Floryan, and A. J. Smits, "Scaling and performance of simultaneously heaving and pitching foils," *AIAA J.* **57**, 3666–3677 (2019).
- ³⁵D. A. Read, F. S. Hover, and M. S. Triantafyllou, "Forces on oscillating foils for propulsion and maneuvering," *J. Fluids Struct.* **17**, 163–183 (2003).
- ³⁶F. Hover, Ø. Haugsdal, and M. Triantafyllou, "Effect of angle of attack profiles in flapping foil propulsion," *J. Fluids Struct.* **19**, 37–47 (2004).
- ³⁷S. Taneda and Y. Tomonari, "An experiment on the flow around a waving plate," *J. Phys. Soc. Jpn.* **36**, 1683–1689 (1974).
- ³⁸T. Kinsey and G. Dumas, "Parametric study of an oscillating airfoil in a power-extraction regime," *AIAA J.* **46**, 1318–1330 (2008).
- ³⁹A. K. Soti, J. Zhao, M. C. Thompson, J. Sheridan, and R. Bhardwaj, "Damping effects on vortex-induced vibration of a circular cylinder and implications for power extraction," *J. Fluids Struct.* **81**, 289–308 (2018).
- ⁴⁰R. Blickhan, C. Krick, D. Zehren, W. Nachtigall, and T. Breithaupt, "Generation of a vortex chain in the wake of a subundulatory swimmer," *Naturwissenschaften* **79**, 220–221 (1992).
- ⁴¹M. H. Dickinson, C. T. Farley, R. J. Full, M. A. R. Koehl, R. Kram, and S. Lehman, "How animals move: An integrative view," *Science* **288**, 100–106 (2000).
- ⁴²R. Godoy-Diana, J. L. Aider, and J. Wesfreid, "Transitions in the wake of a flapping foil," *Phys. Rev. E* **77**, 016308 (2008).
- ⁴³L. Chao, M. M. Alam, and C. Ji, "Drag-thrust transition and wake structures of a pitching foil undergoing asymmetric oscillation," *J. Fluids Struct.* **103**, 103289 (2021).